# Investigation of vortex shedding behind a porous square cylinder using lattice Boltzmann method

V. Babu and Arunn Narasimhan

Citation: Physics of Fluids (1994-present) **22**, 053605 (2010); doi: 10.1063/1.3407667
View online: http://dx.doi.org/10.1063/1.3407667
View Table of Contents: http://scitation.aip.org/content/aip/journal/pof2/22/5?ver=pdfcov
Published by the AIP Publishing

# Investigation of vortex shedding behind a porous square cylinder using lattice Boltzmann method

V. Babu[a] and Arunn Narasimhan[b]
*Department of Mechanical Engineering, Indian Institute of Technology, Madras, Chennai 600036, India*

(Received 14 October 2009; accepted 4 March 2010; published online 24 May 2010)

Incompressible, two-dimensional flow around a porous square cylinder placed in an infinite stream is simulated using the d2q9i model of the lattice Boltzmann method. The Reynolds number (based on the height of the cylinder) is kept at 100. The porosity $\phi$ of the cylinder is varied from 0.25 to 0.9 and permeability through the Darcy number Da from 0.0001 to 0.1. The velocity data at a point downstream of the cylinder are collected at each time step. Discrete Fourier transform analysis of this data is carried out to extract the dominant frequencies of the unsteady flow field behind the cylinder. Strouhal numbers (St) calculated using these dominant frequencies are compared with those of corresponding solid cylinder to bring out the effect of the porous medium on the wake structure and the vortex shedding. At Re=100, as the nondimensional permeability Da is increased from the solid cylinder limit, more flow results through the porous cylinder. The reduction in the value of the dominant frequency with increasing porous medium permeability Da and porosity $\phi$ indicates a substantial reduction in the vortex shedding. Corresponding static pressure plots and St values corroborate this observation at Re=100 and 200. © *2010 American Institute of Physics*. [doi:10.1063/1.3407667]

## I. INTRODUCTION

Numerical simulations of the unsteady flow in the wake of rectangular cylinders immersed in an infinite stream have been widely studied. Davis and Moore[1] numerically investigated the vortex shedding behind rectangles using finite difference methods for Reynolds numbers up to 2800. They compared the numerically computed values of Strouhal numbers (for $Re<1000$) with experimental results. Franke *et al.*[2] performed numerical calculations of flow around square cylinders using finite volume techniques for Reynolds numbers up to 300. The power spectra of the time varying drag and lift coefficients from these calculations showed a dominant frequency as reported by Davis and Moore,[1] but for Reynolds numbers as low as 250, there were noticeable peaks at other frequencies as well. Detailed experimental measurements of the vortex shedding in the wake of square and rectangular cylinders were performed by Okajima[3] for Reynolds numbers between 70 and 10 000. For the square cylinder the Strouhal number increased sharply from 0.1 to 0.15 for Reynolds numbers ranging between 70 and 100 and then stayed within a narrow band of 0.13–0.15 for Reynolds numbers up to 20 000. For rectangular cylinders with aspect ratios (defined as the ratio of the length along the flow direction divided by the height of the cylinder) 2 and 3, the unsteady flow field showed abrupt changes in the value of the Strouhal numbers (mode shifts) as the Reynolds number was varied. For cylinders with aspect ratio 4 the Strouhal number was more or less independent of the Reynolds number. Numerical calculations of this flow were performed by Okajima[4] for Reynolds numbers up to 800 using finite difference methods.

Since the advent of discrete lattice kinetic theory and in particular lattice Boltzmann method (LBM) for solving the Navier–Stokes equations,[5] scores of important isothermal flow simulations have been performed using LBM. They have been reviewed in the excellent monograph by Succi.[6] Simulations of the unsteady flow around a square cylinder situated between two parallel planes using finite volume and the traditional LBM were performed by Bruer *et al.*[7] for flows up to Re=800. The interpolation supplemented lattice Boltzmann (ISLB) proposed by He *et al.*[8] allowed nonuniform meshes to be used in the lattice Boltzmann calculations which were, until then, limited to uniform Cartesian meshes. This enabled higher Reynolds numbers to be simulated without an enormous increase in the computational requirements, as shown by Baskar and Babu[9] who simulated the unsteady flow for the same range of Reynolds numbers studied experimentally by Okajima.[3] The method was later successfully employed in Ref. 10 to simulate high Rayleigh number enclosure convection. An alternative approach for using nonuniform meshes, based on the concept of hierarchical grid refinement, was proposed by Filippova and Hanel.[11,12] However, the former approach is easier to implement as it requires only a simple modification of the traditional lattice-BGK procedure for simulating incompressible flows.

The objective of the present work is to study the effect of a porous square cylinder on the wake structure and vortex shedding frequency. A lattice Boltzmann model for simulating flow through porous media with the linear and nonlinear velocity drag terms (the viscous and form drag terms respectively) included was proposed by Guo and Zhao.[13] An im-

[a]Electronic mail: vbabu@iitm.ac.in.
[b]Author to whom correspondence should be addressed. Electronic mail: arunn@iitm.ac.in. Telephone: +91-44-22574696.

 

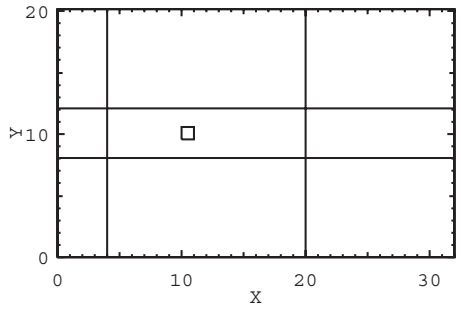


FIG. 1. Computational domain and schematic of the grid.

proved version of this model is used in the present work along with the interpolation supplemented LBM.

## II. PROBLEM DESCRIPTION

Consider a rectangular cylinder of height $H$ and length $L$ placed in a uniform stream as shown in Fig. 1 (for convenience, $H=1$ and $L=2H$ in the figure). Although the aim is to simulate flow around the cylinder when it is placed in an infinite stream, for practical reasons, the computational domain shown in Fig. 1 was limited to a rectangular region $32H\times 20H$. This results in an acceptable blockage ratio of 5%.[9] The center of the cylinder was located on the horizontal centerline of the computational domain at a distance of $10.5H$ from the inlet boundary. Unsteady velocity data were collected at a point $10H$ downstream of the cylinder and $5H$ above the centerline (shown as a filled circle in Fig. 1).

## III. SOLUTION METHODOLOGY

### A. d2q9 model

The 9 bit lattice-BGK model (called the d2q9) for porous media was proposed by Guo and Zhao,[13] which was later used by Wu *et al.*[14] for isothermal flows in porous media and by Seta *et al.*[15] to simulate natural convection in porous media. In this d2q9 model, each node of the lattice is populated by three kinds of particles: a rest particle that resides in the node, particles that move in the coordinate directions, and particles that move in the diagonal directions. The total number of particles in each node in this model is nine. The speed of the particles is such that they move from one node to another during each time step. These speeds can be written as

$$\mathbf{e}_i=\begin{cases}0, & i=0,\\ c\{\cos[(i-1)\pi],\sin[(i-1)\pi]\}, & i=1,2,3,4,\\ \sqrt{2}c\{\cos[(i-5)\pi/2+\pi/4],\sin[(i-5)\pi/2+\pi/4]\}, & i=5,6,7,8.\end{cases} \tag{1}$$

Here $c=\delta_x/\delta_t$, where $\delta_x$ and $\delta_t$ are the lattice spacing and the time step respectively. In the traditional LB method the particles at each node undergo collision followed by advection. In terms of distribution functions, this can be written as

$$f_i(\mathbf{x}+\mathbf{e}_i\delta_t,t+\delta_t)-f_i(\mathbf{x},t) = -\frac{1}{\tau}[f_i(\mathbf{x},t)-f_i^{(eq)}(\mathbf{x},t)]+\delta_t F_i,\quad 0\le i\le 8, \tag{2}$$

where $\tau$ is the dimensionless collisional relaxation time and is related to the kinematic viscosity $\nu$ of the lattice fluid as

$$\nu=\frac{(2\tau-1)}{6}\frac{\delta_x^2}{\delta_t}, \tag{3}$$

and $F_i$ is the force term that accounts for drag effects due to the presence of the porous medium. This can be written as[13]

$$F_i=w_i\rho\left(1-\frac{1}{2\tau}\right)\left[3\frac{\mathbf{e}_i\cdot\mathbf{F}}{c^2}+\frac{9}{\phi}\frac{(\mathbf{e}_i\cdot\mathbf{u})(\mathbf{e}_i\cdot\mathbf{F})}{c^4}-\frac{3}{\phi}\frac{\mathbf{u}\cdot\mathbf{F}}{c^2}\right], \tag{4}$$

where $\phi$ is the porosity. Here, $\mathbf{F}$ is the body force due to the presence of the porous medium and is given as[13]

$$\mathbf{F}=-\frac{\phi\nu}{K}\mathbf{u}-\frac{\phi c_F}{\sqrt{K}}|\mathbf{u}|\mathbf{u}+\phi\mathbf{G}, \tag{5}$$

where $\nu$ is the kinematic viscosity of the fluid, $K$ is the permeability, $c_F$ is the nondimensional Forchcheimer form-drag coefficient, and $\mathbf{G}$ is the body force due to gravity. The first term in this equation, which is linear in velocity, is the viscous drag term and the second term, which is quadratic in velocity, is the form drag term. Owing to the low velocities encountered (Re=100 and 200), in the present work, the viscous drag term alone is retained and the second and the third terms are neglected. Thus,

$$F_i=-\frac{\phi\nu}{K}w_i\rho\left(1-\frac{1}{2\tau}\right)\times\left[3\frac{\mathbf{e}_i\cdot\mathbf{u}}{c^2}+\frac{9}{\phi}\frac{(\mathbf{e}_i\cdot\mathbf{u})^2}{c^4}-\frac{3}{\phi}\frac{\mathbf{u}\cdot\mathbf{u}}{c^2}\right],\quad 0\le i\le 8, \tag{6}$$

Eq. (2) above describes the evolution of the LB automaton. The equilibrium functions that appear in the right hand side of this equation can be evaluated[13] as follows:

TABLE I. Values used for porosity and Darcy number.

| | $\phi$ | | | |
|---|---|---|---|---|
| Da | 0.25 | 0.5 | 0.75 | 0.9 |
| 0.1 | ⋯ | ⋯ | ⋯ | √ |
| 0.01 | ⋯ | ⋯ | √ | √ |
| 0.001 | ⋯ | √ | √ | √ |
| 0.0001 | √ | √ | √ | √ |

$$f_i^{(eq)} = w_i\rho\left[1 + 3\frac{\mathbf{e}_i\cdot\mathbf{u}}{c^2} + \frac{9}{2\phi}\frac{(\mathbf{e}_i\cdot\mathbf{u})^2}{c^4} - \frac{3}{2\phi}\frac{\mathbf{u}\cdot\mathbf{u}}{c^2}\right], \quad 0 \le i \le 8, \tag{7}$$

where $w_0=4/9$, $w_i=1/9$ for $i=1,2,3,4$, and $w_i=1/36$ for $i=5,6,7,8$. Also, $\rho$ is the density and $\mathbf{u}$ is the velocity of the fluid. These are given as

$$\rho = \sum_{i=0}^{8} f_i, \tag{8}$$

$$\rho\mathbf{u} = \sum_{i=1}^{8} \mathbf{e}_i f_i + \frac{\delta_t}{2}\rho\mathbf{F}. \tag{9}$$

If we substitute for $\mathbf{F}$ from Eq. (5), we get

$$\rho\mathbf{u} = \sum_{i=1}^{8} \mathbf{e}_i f_i - \frac{\delta_t}{2}\frac{\phi\nu}{K}\rho\mathbf{u}. \tag{10}$$

### B. d2q9i model

In the LBM, the pressure is calculated using an equation of state. Pressure and density are related through the speed of sound as

$$p = c_s^2\rho, \tag{11}$$

where $c_s=c/\sqrt{3}$ is the speed of sound. The entire governing equations can be written in terms of pressure rather than density using the above equation so that the pressure field can be obtained directly.[8] This is the d2q9i model that has been used in the present work.[9] Another advantage of this approach is that the incompressible Navier–Stokes equations can be recovered from the LB equations to within $O(\mathrm{Ma}^2)$ where Ma is the Mach number, in contrast with the d2q9 model which recovers the incompressible N-S equations only to within $O(\mathrm{Ma})$. The derivation of the working equations for the d2q9i model follows.

Upon multiplying Eq. (2) by $c_s^2$ and defining $p_i=c_s^2 f_i$, we get

$$p_i(\mathbf{x}+\mathbf{e}_i\delta_t, t+\delta_t) - p_i(\mathbf{x},t) = -\frac{1}{\tau}[p_i(\mathbf{x},t) - p_i^{(eq)}(\mathbf{x},t)] + \delta_t c_s^2 F_i, \quad 0 \le i \le 8. \tag{12}$$

Since the flow is incompressible, the density is essentially constant but with small fluctuations, *viz.*, $\rho=\rho_0+\delta\rho$. The quantity $\rho_0$ can be thought of as a reference density and it has been conveniently taken to be equal to 1 in the present work. The exact value used for $\rho_0$ is immaterial as the solution obtained is independent of this value. It should be noted that $\delta\rho$ is $O(\mathrm{Ma}^2)$ in the incompressible limit.

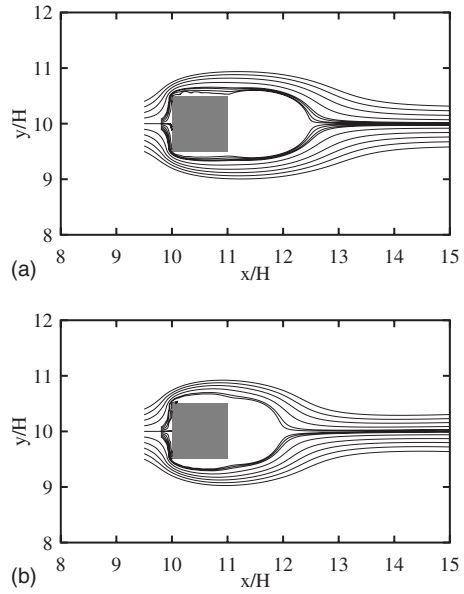


FIG. 2. Validation result: streamlines around solid block for (a) Re=100 and (b) Re=200.

The equilibrium functions that appear in the right hand side of Eq. (12) can be evaluated by first multiplying both sides of Eq. (7) by $c_s^2$ and then substituting for $\rho$. After neglecting product terms like $\delta\rho(\mathbf{u}/c)$ and $\delta\rho(\mathbf{u}/c)^2$, which are actually $O(\mathrm{Ma}^3)$ and $O(\mathrm{Ma}^4)$, we get

$$p_i^{(eq)} = w_i\left[p + \rho_0(\mathbf{e}_i\cdot\mathbf{u}) + \frac{3\rho_0}{2\phi}(\mathbf{e}_i\cdot\mathbf{u})^2 - \frac{\rho_0}{2\phi}\mathbf{u}\cdot\mathbf{u}\right], \quad 0 \le i \le 8, \tag{13}$$

where $p$ is the pressure as defined above. In a similar manner, it is easy to show from Eqs. (6), (8), and (10) that

$$F_i = -\frac{\phi\nu}{K}w_i\rho_0\left(1-\frac{1}{2\tau}\right)\times\left[3\frac{\mathbf{e}_i\cdot\mathbf{u}}{c^2} + \frac{9}{\phi}\frac{(\mathbf{e}_i\cdot\mathbf{u})^2}{c^4} - \frac{3}{\phi}\frac{\mathbf{u}\cdot\mathbf{u}}{c^2}\right], \quad 0 \le i \le 8, \tag{14}$$

and

$$p = \sum_{i=0}^{8} p_i, \tag{15}$$

and

$$\rho_0\mathbf{u} = \frac{1}{c_s^2}\sum_{i=1}^{8}\mathbf{e}_{ii}p_i - \frac{\delta_t}{2}\frac{\phi\nu}{K}\rho_0\mathbf{u}. \tag{16}$$

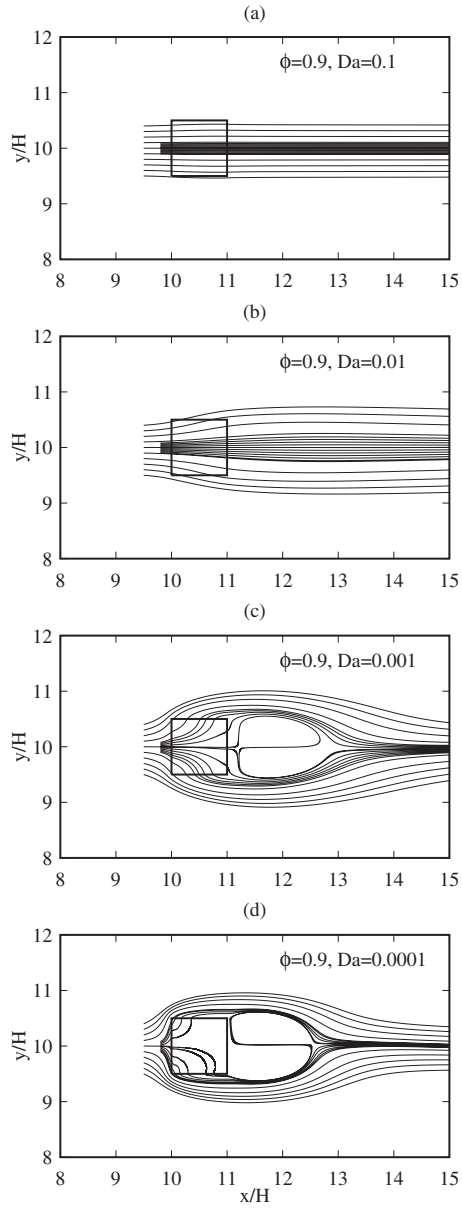


FIG. 3. Streamlines for time averaged mean flow in porous block at Re=100, $\phi$=0.9, (a) Da=$10^{-1}$, (b) Da=$10^{-2}$, (c) Da=$10^{-3}$, and (d) Da=$10^{-4}$.

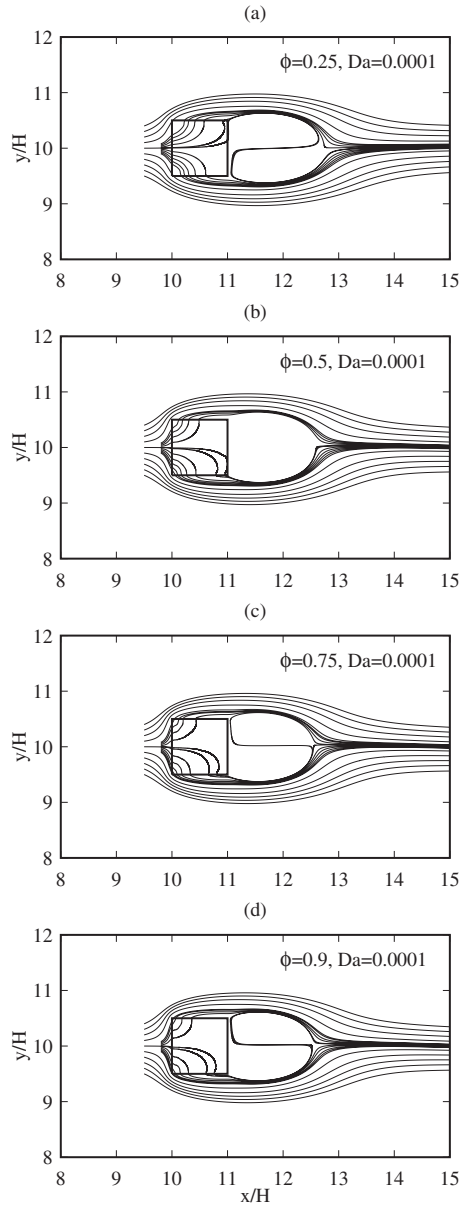


FIG. 4. Streamlines for time averaged mean flow in porous block at Re=100, Da=$10^{-4}$, (a) $\phi$=0.25, (b) =0.50, (c) =0.75, and (d) =0.9.

### C. Implementation on nonuniform grid

In the ISLB method, the lattice Boltzmann automaton is assumed to reside on a *uniform lattice* with spacing equal to $\delta_x$. During each time step, the particles on this *lattice* undergo collision followed by advection as dictated by the lattice-BGK model.[8] However, the particle distribution functions $f_i$ (and hence the density $\rho$ and velocity $\mathbf{u}$) are evaluated on the nodes of a *computational grid* overlaid on the lattice. The nodes of the computational grid need not coincide with the nodes of the lattice and after advection on the lattice the particles can be off node. The particle distribution function at each node of the *computational grid* can then be determined by using second order accurate Lagrangian interpolation.[8] This is, however, not required in regions where the spacing of the computational grid equals the lattice spacing. The particle distributions on the boundary nodes of the *computational grid* are then modified according to the imposed boundary conditions. On the top and bottom boundaries, which are zero-shear boundaries, slip boundary condition is imposed using the particle reflection rule. At the inlet, the particle distribution functions are set equal to the corresponding equilibrium distributions. At the exit, the particles are simply allowed to leave the domain.

The Cartesian *computational grid* used for the present calculations (Fig. 1) consists of several zones in the $x$ and $y$ directions. The innermost zone surrounding the cylinder is a uniform grid with equal spacing in both the coordinate directions. The spacing of the grid in this zone is the finest in the entire domain. The spacing of the grid in the outer zone is twice that of the inner zone. The outlines of the zones for the grid with two levels in the $x$ direction and two levels in the $y$ direction are shown in Fig. 1.

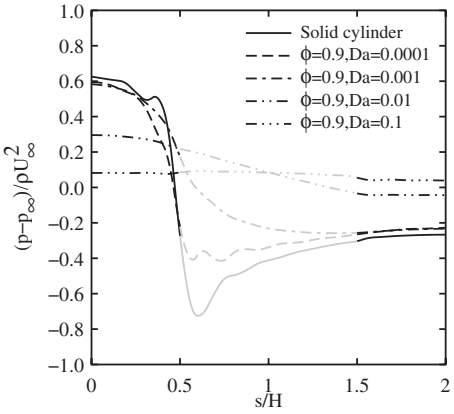


FIG. 5. Variation of dimensionless static pressure $C_p$ along the upper half of the cylinder at Re=100, $\phi$=0.9 for several Da values.

### D. Dimensionless parameters

With the height of the cylinder as the characteristic length and the freestream velocity $u_\infty$ as the characteristic velocity, the relevant dimensionless parameters are Reynolds number, Re(=$u_\infty H/\nu$), Darcy number, Da(=$K/H^2$), and porosity $\phi$. Since the flow simulated by the LB method is weakly compressible, Mach number, Ma(=$u_\infty/c$), is also a relevant parameter. Based on the values for these parameters, values for $u_\infty$, $\tau$, and $K$ for simulations on the lattice can be determined as follows. From the definition of Mach number, it is easy to see that $u_\infty$=Ma $c$.

The Reynolds number can be written as

$$\mathrm{Re} = \frac{u_\infty H}{\nu} = \frac{\mathrm{Ma}\, cN\delta_x}{\nu}, \tag{17}$$

where $N$ is the number of *lattice* nodes along the characteristic length. Upon using Eq. (3) and rearranging, we get

$$\tau = \frac{1}{2} + \frac{3\ \mathrm{Ma}\ N}{\mathrm{Re}}. \tag{18}$$

The permeability $K$ of a porous medium made of packed spherical particles is related to the volumetric porosity $\phi$ and characteristic pore length scale through the Carman–Kozeny relationship.[16] In nondimensional form this empirical relation can be written as

$$\mathrm{Da} = \frac{K}{H^2} = \frac{1}{180}\frac{\phi^3 (D_p)^2}{H^2(1-\phi)^2}. \tag{19}$$

The above relation is used as a guideline to arrive at suitable $K$ and $\phi$ combinations that yield porous media with physically realistic pore scales $D_p$ not exceeding $H$, the characteristic porous cylinder size. In light of Eq. (19), for a chosen Da, since $H$ is also fixed, the pore scale $D_p$ changes correspondingly when $\phi$ is varied. Table I provides the possible combinations within the range $10^{-4} \le \mathrm{Da} \le 10^{-1}$ and $0.25 \le \phi \le 0.9$. Porosity and Darcy number are set to 1 and $10^{20}$, respectively, in the clear fluid region.

Reynolds numbers tested are 100 and 200 ensuring the flow is kept two dimensional. The Mach number is kept fixed at 0.1. In all simulations, $N$ is equal to 16, an adequate value[9] for this range of Reynolds numbers. Since the flow is un-

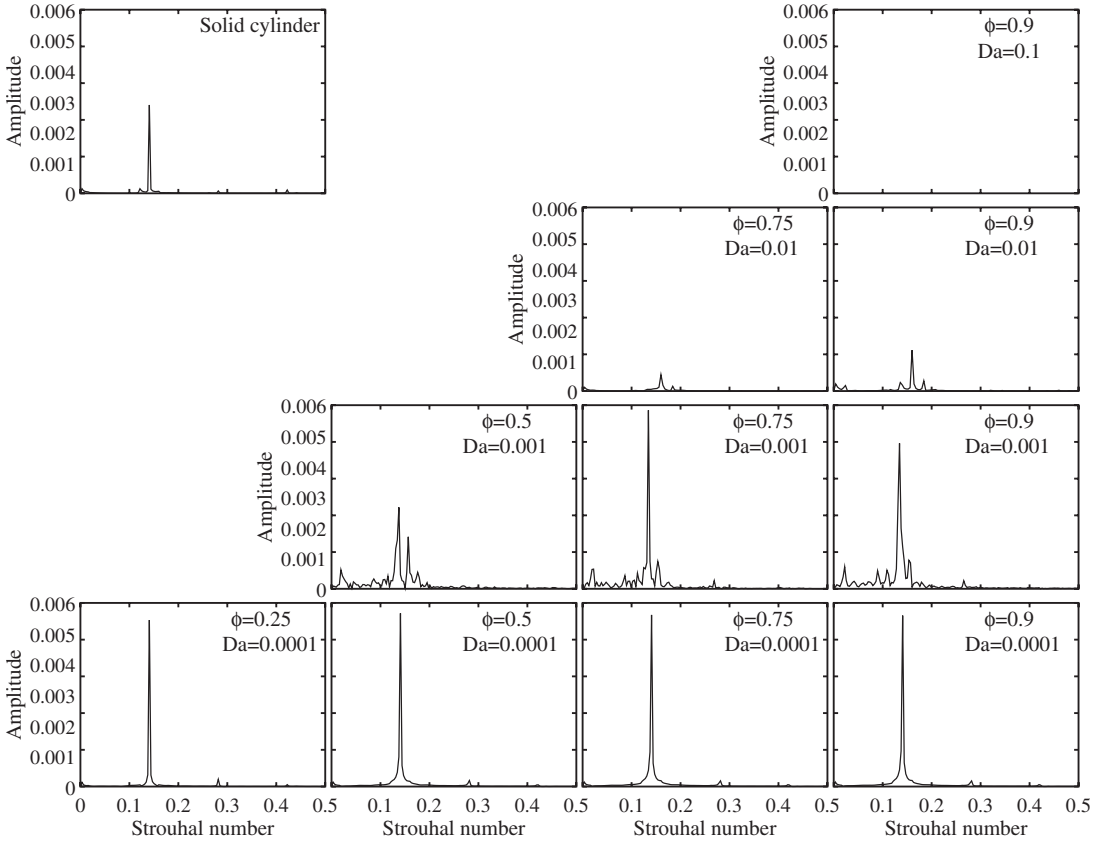


FIG. 6. Frequency spectra at Re=100 for all physically realizable porous media from Table I.

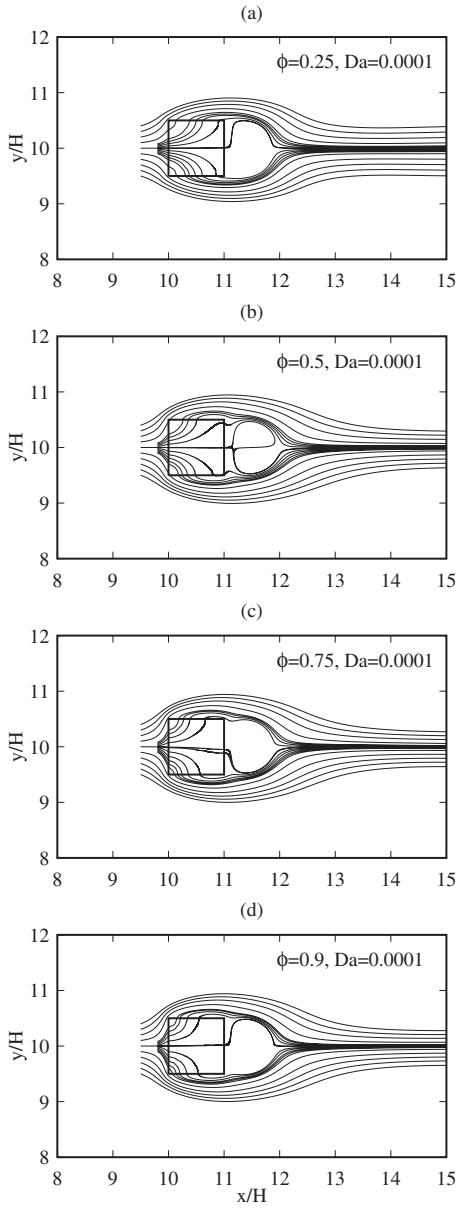


FIG. 7. Streamlines for time averaged mean flow in porous block at at Re=200, Da=$10^{-4}$, (a) $\phi$=0.25, (b) =0.50, (c) =0.75, and (d) =0.90.

steady, during postprocessing, another dimensionless quantity, the Strouhal number, has to calculated. It is customary to define the Strouhal number, St, as $fH/u_\infty$, where $f$ is the frequency in Hertz. For lattice calculations, it is easy to show that

$$\mathrm{St} = fN/\mathrm{Ma}, \tag{20}$$

where $f$ is the frequency in lattice units.

Discrete Fourier transform (DFT) of the unsteady velocity data collected at a point downstream of the cylinder is performed to extract the dominant frequencies of the unsteady flow field behind the cylinder. St values calculated using these dominant frequencies and corresponding streamlines for several porous cylinder configurations are analyzed to reveal the effect of the porous medium on the wake structure and vortex shedding.

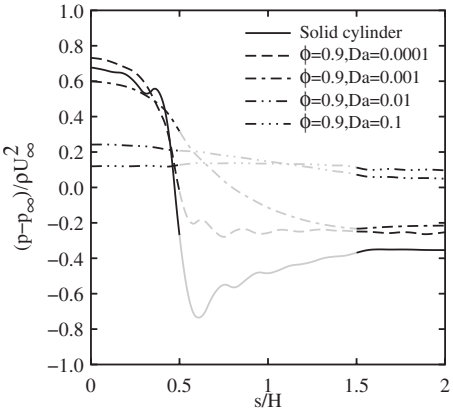


FIG. 8. Variation of dimensionless static pressure $C_p$ along the upper half of the cylinder at Re=200, $\phi$=0.9 for several Da values.

## IV. RESULTS AND DISCUSSION

In Table I, the marked pairs indicate the combination of volumetric porosity $\phi$ and nondimensional permeability Da that yields physically realizable porous media, satisfying the Carmen–Kozeny relationship, Eq. (19). For fixed Re=100 and porosity $\phi$=0.9, the effect of permeability Da variation on the flow around the porous block is brought out through streamlines of the time-averaged mean flow in Fig. 3. In Fig. 3(a), since the nondimensional permeability is very high Da=0.01, the streamlines are nearly undisturbed across the control volume around the porous block. As Da decreases by successive orders in frames of Figs. 3(a)–3(d), due to the corresponding increase in the porous medium viscous drag, reduced flow is observed within the porous block. The streamlines of Fig. 3(d) are almost identical to those for the solid block case shown in Fig. 2(b).

Reducing the porosity, in principle, reduces the flow volume (area, in the present case) within the porous block. Thus, from Eq. (19), the pore size $D_p$ changes for a fixed Da. However nondimensional the permeability Da has to be low when the porosity is reduced in order to achieve physically realizable porous media as shown in Table I. This ensures the viscous drag inside the porous block to predominate. Therefore, compared to the identical Da values from Fig. 3, the effect of porosity reduction on the streamlines is observed to be minor in Fig. 4, where, for fixed Da=0.0001, the effect of $\phi$ on the streamlines through physically realizable porous block (bottommost row in Table I) is shown.

The variation of the dimensionless static pressure $C_p$ $[=(p-p_\infty)/(\rho U_\infty^2)]$ along the upper half of the cylinder is shown in Fig. 5 for $\phi$=0.9 and several permeability Da values. Here $p_\infty$ is the reference, free stream, static pressure, $\rho$, the density, and $U_\infty$, the free stream velocity of the fluid. The upper half consists of three sides, namely, the upstream side $(x/H=10, 10\le y/H<10.5)$, the top surface $(10\le x/H\le 11, y/H=10.5)$, and the downstream side $(x/H=11, 10.5>y/H\ge 10)$. In this plot, the abscissa is the nondimensional distance along the surface starting from the front stagnation point. In the plot, the pressure variation on the upstream and downstream sides of the cylinder is shown in dark curves while that of the top surface is shown in gray since this does

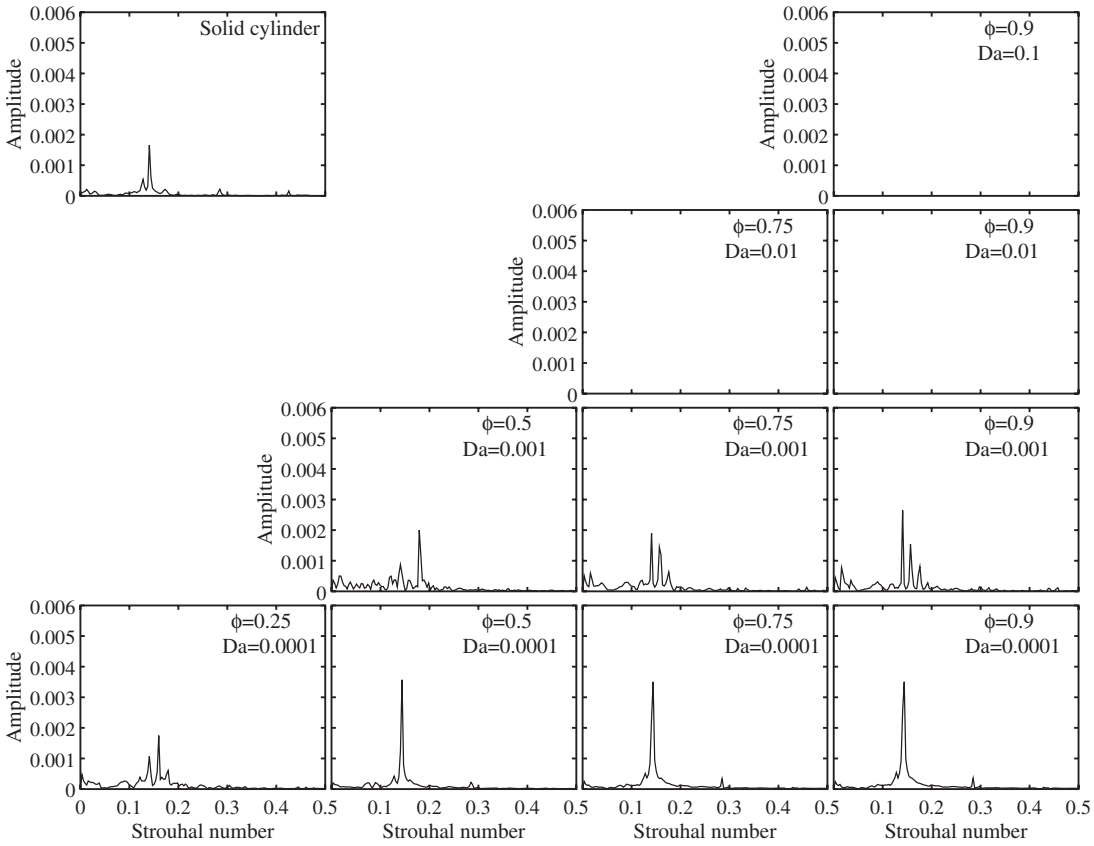


FIG. 9. Frequency spectra at Re=200 for all physically realizable porous media from Table I.

not contribute to the pressure drag. The pressure drop incurred by the solid cylinder is expectedly the highest. As Da increases, a sharp drop in the momentum change across the porous cylinder is observed. For Da=0.1, the pressure drop is almost negligible suggesting through-flow in the porous cylinder.

Strouhal number provides the measure for the intrinsic oscillatory flow instability occurring with steady state boundary conditions. Figure 6 shows the amplitude and frequency spectra of St values at Re=100 for flow around each of the physically realizable porous blocks from Table I. For reference, the St spectra for flow around a solid cylinder are also shown at the top left corner. The single sharp spectral peak at the predominant frequency indicates the onset of strong vortex shedding in the wake and has been well documented in reported literature. The bottommost row of St spectra is for the porous block case at the lowest block nondimensional permeability Da=0.0001 and for several porosities. Since the Da=0.0001 is very low, the distinct peak at a predominant frequency nearly matches that of the solid cylinder case. Moreover, the predominant frequency value is also nearly the same as that of the solid cylinder case, reiterating the negligible effect of porosity. This observation corroborates the nearly identical pressure drop incurred by such porous blocks in Fig. 5, when compared with the solid block case.

From this lowest Da bottom row, as one proceeds in Fig. 6 to the top with progressive increase in Da values, it is evident that the sharp peak at the predominant frequency reduces in amplitude. This suggests a reduction in vortex shedding in the wake of the corresponding high permeable porous blocks. The reduction in pressure drop across these porous blocks of higher permeability in Fig. 5 also indicates the same. As observed from the streamlines presented earlier, since there is flow through the porous blocks at the downstream face, the strength of the local shear flow near the trailing edges of the square face is reduced. Consequently the onset of vortex shedding for Re=100 is expected to subside with increased porous block permeability. Supporting this reasoning, in Fig. 6, the topmost row for Da=0.1 (and $\phi$=0.9) registers no significant peak at any predominant St frequency.

Clarifying a point raised by one reviewer, it is worth recalling at this stage that the limiting process Da$\rightarrow$0 and $\phi\rightarrow$0 of Eqs. (4) and (5) does not recover the solid cylinder limit. This is an inherent limitation of the porous media formulation using LBM. The solid cylinder results reported are obtained by solving the clear fluid LBM equation. This is one possible explanation for the solid cylinder case not to have the highest peak/amplitude in Fig. 6.

In addition, a recent work[17] discussed the discrepancy in the effective viscosity predicted by LBM and the Chapman–Enskog expansion. The LBM and porous medium parameters must be chosen properly to avoid any discrepancy in the effective viscosity predicted by these two formulations. Assuaging concerns regarding this, the parameters in our presented formulation have indeed been chosen properly so that the ratio of effective viscosity to kinematic viscosity is unity, which does not result in any discrepancy. Further, the value

of $N$ used in the present study is shown to be adequate for the range of Reynolds number considered, in Ref. 9. A grid independence study has been carried out for the porous medium formulation and the differences in the predictions for small $K$ values have been found to be small.

At Re=200, similar trend of flows, wake structure, and Strouhal number behavior are observed. For instance, in Fig. 7, for $Da=10^{-4}$, the effect of porosity on the streamlines resembles that at Re=100 in Fig. 4. The $C_p$ plot in Fig. 8 also resembles that for Re=100 in Fig. 5, with the expected increase in the $C_p$ magnitudes. Interestingly, for Da=0.01 and Da=0.1, the pressure drop magnitudes for both Re=100 and Re=200 are almost identical. Figure 9 depicts the amplitude and frequency spectra of St values at Re=200 for the entire physically realizable porous blocks from Table I. Only for the lowest $Da=10^{-4}$ value, unique amplitude peaks are observable. As Da increases, irrespective of the porosity value, the amplitude peaks are observed to scatter and spread out and disappear.

As indicated earlier, for the solid cylinder, Da=0 and, hence, both Da and $\phi$ disappear completely. To obtain solid cylinder results, the LBE corresponding to the clear fluid alone is solved. Although the case of Da=0.0001 is close to that of the solid cylinder case (Da=0), only the LBE with nonzero porous media terms is solved for obtaining the St results. Hence, combinations wherein the porosity is high but the permeability is low (as in Fig. 8) result in slightly different predictions on the surface of the cylinder than that of the solid cylinder. These differences can be ignored without losing generality while interpreting the results.

## V. CONCLUSIONS

The phenomenon of vortex shedding from a two-dimensional porous square cylinder placed in an infinite incompressible flow stream is simulated in detail using the d2q9i model of the LBM. Satisfying the Carmen–Kozeny relation, suitable combination of permeability $10^{-4} \leq Da \leq 10^{-1}$ and porosity $0.25 \leq \phi \leq 0.9$ values are chosen for the realistic porous media of the square cylinder.

For Re=100 and 200, the effect of Da and $\phi$ on the vortex shedding is characterized using the Strouhal number St of the configuration. At Re=100, as the permeability Da is increased from the solid cylinder limit, streamlines indicate progressively more flow through the porous cylinder. As a result, the strength of the vortex shedding from the trailing edge of the porous square cylinder is observed to reduce. The progressive reduction and absence of dominant frequency for increasing porous medium nondimensional permeability Da the DFT analysis also corroborate the reduction in the vortex shedding. Corresponding St values also indicate the same.

A similar trend of wake structure, reduction in dominant frequency, and vortex shedding for progressive increase in Da and $\phi$ is observed for Re=200. Further analysis at higher Re is required to delineate the three-dimensional unsteady effects to shape the proposed concept as a possible technique for suppression of vortex shedding in engineering applications.

[1] R. W. Davis and E. F. Moore, "A numerical study of vortex shedding from rectangles," J. Fluid Mech. **116**, 475 (1982).
[2] R. Franke, W. Rodi, and B. Schönung, "Numerical calculation of laminar vortex-shedding flow past cylinders," J. Wind. Eng. Ind. Aerodyn. **35**, 237 (1990).
[3] A. Okajima, "Strouhal numbers of rectangular cylinders," J. Fluid Mech. **123**, 379 (1982).
[4] A. Okajima, "Numerical simulation of flow around rectangular cylinders," J. Wind. Eng. Ind. Aerodyn. **33**, 171 (1990).
[5] S. Chen and G. D. Doolen, "Lattice Boltzmann method for fluid flows," Annu. Rev. Fluid Mech. **30**, 329 (1998).
[6] S. Succi, *Lattice Boltzmann Method for Fluid Dynamics and Beyond* (Oxford University Press, New York, 2001).
[7] M. Breuer, J. Bernsdorf, T. Zeiser, and F. Durst, "Accurate computations of the laminar flow past a square cylinder based on two different methods: Lattice-Boltzmann and finite-volume," Int. J. Heat Fluid Flow **21**, 186 (2000).
[8] X. He, L.-S. Luo, and M. Dembo, "Some progress in lattice Boltzmann method. Part I. Nonuniform mesh grids," J. Comput. Phys. **129**, 357 (1996).
[9] G. Baskar and V. Babu, "Simulation of the unsteady flow around rectangular cylinders using the ISLB method," AIAA Paper No. 2004-2651, 2004.
[10] H. N. Dixit and V. Babu, "Simulation of high Rayleigh number natural convection in a square cavity using the lattice Boltzmann method," Int. J. Heat Mass Transfer **49**, 727 (2006).
[11] O. Filippova and D. Hanel, "Grid refinement for lattice-BGK models," J. Comput. Phys. **147**, 219 (1998).
[12] O. Filippova and D. Hanel, "Acceleration of lattice-BGK schemes with grid refinement," J. Comput. Phys. **165**, 407 (2000).
[13] Z. Guo and T. S. Zhao, "Lattice Boltzmann model for incompressible flows through porous media," Phys. Rev. E **66**, 036304 (2002).
[14] H. R. Wu, Y. L. He, G. H. Tang, and W. Q. Tao, "Lattice Boltzmann simulation of flow in porous media on non-uniform grids," Prog. Comput. Fluid Dyn. **5**, 97 (2005).
[15] T. Seta, E. Takegoshi, and K. Okui, "Lattice Boltzmann simulation of natural convection in porous media," Math. Comput. Simul. **72**, 195 (2006).
[16] D. A. Nield and A. Bejan, *Convection in Porous Media*, 3rd ed. (Springer, New York, 2006).
[17] X. Nie and N. S. Martys, "Breakdown of Chapman–Enskog expansion and the anisotropic effect for lattice-Boltzmann models of porous flow," Phys. Fluids **19**, 011702 (2007).